

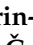




Article

Grain-Size-Induced Collapse of Variable Range Hopping and Promotion of Ferromagnetism in Manganite $\text{La}_{0.5}\text{Ca}_{0.5}\text{MnO}_3$

Nikolina Novosel ^{1,†}, David Rivas Góngora ^{1,†,‡}, Zvonko Jagličić ^{2,3}, Emil Tafrā ⁴, Mario Basletić ⁴, Amir Hamzić ⁴ , Teodoro Klaser ⁵, Željko Skoko ⁴ , Krešimir Salamon ⁵, Ivna Kavre Piltaver ⁶, Mladen Petravić ⁶, Bojana Korin-Hamzić ¹, Silvia Tomić ¹ , Boris P. Gorshunov ⁷ , Tao Zhang ⁸, Tomislav Ivek ^{1,*} and Matija Čulo ^{1,*} 

- ¹ Institut za fiziku, Bijenička cesta 46, HR-10000 Zagreb, Croatia; nnovosel@ifs.hr (N.N.); d.r.gongora@smn.uio.no (D.R.G.); hamzic.bojana@gmail.com (B.K.-H.); stomic@ifs.hr (S.T.)
 - ² Institute of Mathematics, Physics and Mechanics, Jadranska 19, 1000 Ljubljana, Slovenia; zvonko.jaglicic@imfm.si
 - ³ Faculty of Civil and Geodetic Engineering, University of Ljubljana, Jamova c. 2, 1000 Ljubljana, Slovenia
 - ⁴ Department of Physics, Faculty of Science, University of Zagreb, Bijenička cesta 32, HR-10000 Zagreb, Croatia; etafrā@phy.hr (E.T.); basletic@phy.hr (M.B.); hamzic@phy.hr (A.H.); zskoko@phy.hr (Ž.S.)
 - ⁵ Ruđer Bošković Institute, Bijenička cesta 54, 10000 Zagreb, Croatia; tkklaser@irb.hr (T.K.); kresimir.salamon@irb.hr (K.S.)
 - ⁶ University of Rijeka, Faculty of Physics and Center for Micro- and Nanosciences and Technologies, Radmile Matejčić 2, 51000 Rijeka, Croatia; ivna.kavre@uniri.hr (I.K.P.); mpetravic@uniri.hr (M.P.)
 - ⁷ Laboratory of Terahertz Spectroscopy, Center for Photonics and 2D Materials, Moscow Institute of Physics and Technology, National Research University, 141701 Dolgoprudny, Russia; bpgorshunov@gmail.com
 - ⁸ School of Physics and Materials Sciences, Guangzhou University, Guangzhou 510006, China; zhangtao@gzhu.edu.cn
- * Correspondence: tivek@ifs.hr (T.I.); mculo@ifs.hr (M.Č.)
[†] These authors contributed equally to this work.
[‡] Current address: Department of Physics, University of Oslo, NO-0316 Oslo, Norway.



Citation: Novosel, N.; Rivas Góngora, D.; Jagličić, Z.; Tafrā, E.; Basletić, M.; Hamzić, A.; Klaser, T.; Skoko, Ž.; Salamon, K.; Kavre Piltaver, I.; et al. Grain-Size-Induced Collapse of Variable Range Hopping and Promotion of Ferromagnetism in Manganite $\text{La}_{0.5}\text{Ca}_{0.5}\text{MnO}_3$. *Crystals* **2022**, *12*, 724. <https://doi.org/10.3390/cryst12050724>

Academic Editors: Raghvendra Singh Yadav and Artem Pronin

Received: 16 April 2022

Accepted: 16 May 2022

Published: 19 May 2022

Publisher's Note: MDPI stays neutral with regard to jurisdictional claims in published maps and institutional affiliations.



Copyright: © 2022 by the authors. Licensee MDPI, Basel, Switzerland. This article is an open access article distributed under the terms and conditions of the Creative Commons Attribution (CC BY) license (<https://creativecommons.org/licenses/by/4.0/>).

Abstract: Among transition metal oxides, manganites have attracted significant attention because of colossal magnetoresistance (CMR)—a magnetic field-induced metal–insulator transition close to the Curie temperature. CMR is closely related to the ferromagnetic (FM) metallic phase which strongly competes with the antiferromagnetic (AFM) charge ordered (CO) phase, where conducting electrons localize and create a long range order giving rise to insulator-like behavior. One of the major open questions in manganites is the exact origin of this insulating behavior. Here we report a dc resistivity and magnetization study on manganite $\text{La}_{1-x}\text{Ca}_x\text{MnO}_3$ ceramic samples with different grain size, at the very boundary between CO/AFM insulating and FM metallic phases $x = 0.5$. Clear signatures of variable range hopping (VRH) are discerned in resistivity, implying the disorder-induced (Anderson) localization of conducting electrons. A significant increase of disorder associated with the reduction in grain size, however, pushes the system in the opposite direction from the Anderson localization scenario, resulting in a drastic decrease of resistivity, collapse of the VRH, suppression of the CO/AFM phase and growth of an FM contribution. These contradictory results are interpreted within the standard core-shell model and recent theories of Anderson localization of interacting particles.

Keywords: manganites; colossal magnetoresistance; metal–insulator transition; charge order; grain size; variable range hopping; Anderson localization; core–shell model

1. Introduction

In contrast to conventional materials, valence electrons of transition metal oxides are strongly correlated, giving rise to exotic ordered states such as the Mott insulator, spin density waves, charge order, etc. [1]. Very often, a single material can host more

than one of these states, as well as some conventional phases, which can either coexist or be transformed from one into the other by changing temperature, pressure, doping, or magnetic field. One of the most intriguing is the transition between an insulating and a metallic phase, the two phases so dissimilar that they may be considered as fundamental states of condensed matter. It is therefore not surprising that the transition metal oxides have attracted a lot of attention and are at the heart of condensed matter physics.

Among transition metal oxides, the family of manganese oxides, widely known as manganites, today plays a prominent role within the field of strongly correlated electron systems. Although synthesized in 1950 [2], a major interest for manganites started only in 1994 with the discovery of colossal magnetoresistance (CMR)—a transition close to the Curie point from an insulating to a metallic state caused by a magnetic field [3,4]. For general reviews, see Refs. [5–8].

Manganites can be described by a general formula $R_{1-x}A_x\text{MnO}_3$, where R stands for a trivalent rare earth or Bi^{3+} cation and A for a divalent alkaline earth or Pb^{2+} cation. Substituting R for A results in the realization of many different ordered states, i.e., in rich phase diagrams. The conventional phase diagram of the titular compound $\text{La}_{1-x}\text{Ca}_x\text{MnO}_3$ [9] is shown in Figure 1a. The left part is dominated by a ferromagnetic (FM) ground state which is metallic ($0.2 \lesssim x < 0.5$), and the right part is dominated by an antiferromagnetic (AFM) charge-ordered (CO) ground state which is insulating ($0.5 < x \lesssim 0.9$), indicating a close relationship between magnetic and transport properties. At high temperatures, $\text{La}_{1-x}\text{Ca}_x\text{MnO}_3$ is in a paramagnetic (PM) insulating state for all x . The previously mentioned CMR is tied to the FM metallic part of the phase diagram.

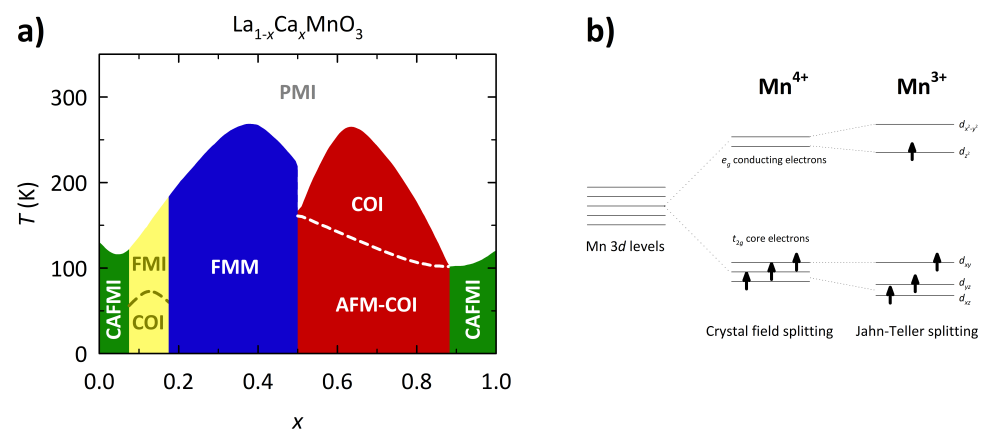


Figure 1. (a) Conventional phase diagram of $\text{La}_{1-x}\text{Ca}_x\text{MnO}_3$. PMI stands for a paramagnetic insulating phase, FMM for a ferromagnetic metallic, COI for a charge-ordered insulating, AFM for an antiferromagnetic, FMI for a ferromagnetic insulating and CAFMI for a canted antiferromagnetic insulating state. This figure is based on data from Ref. [9]. (b) Splitting of the Mn 3d levels into e_g and t_{2g} orbitals by crystal field and Jahn–Teller distortion.

$\text{La}_{1-x}\text{Ca}_x\text{MnO}_3$ should crystallize in the ideal cubic perovskite crystal structure with an Mn atom in the center of the cube, La or Ca atoms at the corners of the cube and O atoms positioned in the center of each cube face. In this way, each Mn atom is octahedrally surrounded by six O atoms. In reality, however, the perovskite structure of $\text{La}_{1-x}\text{Ca}_x\text{MnO}_3$ is distorted, first due to different size of atoms and the pores which they occupy and second due to the Jahn–Teller effect, which leads to the less symmetric orthorhombic crystal structure.

According to simple stoichiometry, pure LaMnO_3 ($x = 0$) contains La^{3+} , Mn^{3+} and O^{2-} , while pure CaMnO_3 ($x = 1$) contains Ca^{2+} , Mn^{4+} and O^{2-} . Density functional theory (DFT) studies [10,11] show that electronic properties of LaMnO_3 and CaMnO_3 are mostly determined by Mn^{3+} and Mn^{4+} , respectively, the only ions with open shells. Mn 3d orbitals are split by the oxygen octahedral field into three t_{2g} orbitals with lower energy (d_{xy} , d_{yz}

and d_{xz}) and two e_g orbitals with higher energy ($d_{x^2-y^2}$ and d_{z^2}) as shown in Figure 1b. The deformation of the MnO_6 octahedron caused by the Jahn–Teller effect leads to an additional splitting of Mn^{3+} e_g orbitals into a higher energy $d_{x^2-y^2}$ and a lower energy d_{z^2} orbital. Mn^{4+} has three electrons which occupy only the t_{2g} orbitals, while Mn^{3+} has one more electron which occupies one of the two e_g orbitals. Due to the Hund coupling, the spins of all electrons are parallel, and each electron occupies a separate orbital, which explains why pure LaMnO_3 and CaMnO_3 are magnetic and insulating.

Substituting La^{3+} for Ca^{2+} introduces the mixed valence state $\text{Mn}^{3+}/\text{Mn}^{4+}$, which opens a conduction channel in $\text{La}_{1-x}\text{Ca}_x\text{MnO}_3$ via hopping of e_g electron between Mn^{3+} and Mn^{4+} . It is therefore useful to distinguish the conducting e_g electrons responsible for charge transport from the core t_{2g} electrons that give rise to a magnetic moment of Mn^{3+} and Mn^{4+} (see Figure 1b). Due to the Hund interaction, the hopping of conducting electrons depends on the angle between the magnetic moments of Mn^{3+} and Mn^{4+} and is maximal (minimal) when the moments are parallel (antiparallel). The effective hopping integral may therefore be written as $t = t_{\max}\cos(\theta/2)$, where t_{\max} is the maximal value and θ the angle between the moments. This, the so called double exchange mechanism [12–14], qualitatively captures the essential features of the $\text{La}_{1-x}\text{Ca}_x\text{MnO}_3$ phase diagram in Figure 1a: the metallic behavior of the FM phase ($\theta = 0$, $t = t_{\max}$), the insulating behavior of the AFM phase ($\theta = \pi$, $t = 0$), and CMR (θ changes in field).

There are several more interactions that govern the physics of manganites. Namely, since an Mn^{3+} octahedron is distorted due to the Jahn–Teller effect, while Mn^{4+} is not, each hop of an e_g electron from Mn^{3+} to Mn^{4+} must be accompanied by a change of local octahedron. Such a strong electron–lattice coupling competes with electron delocalization and is believed to give rise to insulating polaron conduction in the PM state at high temperatures [15–20]. Charge ordering, i.e., a periodic arrangement of Mn^{3+} and Mn^{4+} , points towards localization of e_g electrons due to the nearest-neighbor Coulomb and/or Jahn–Teller interaction [21–27], which induces the periodic arrangement of e_g d_{z^2} orbitals as well [9,24,28,29]. Finally, there is a superexchange interaction between neighboring core t_{2g} electrons that favors AFM alignment of the Mn magnetic moments and directly competes with the FM double exchange [30–33].

The transport and magnetic properties of $\text{La}_{1-x}\text{Ca}_x\text{MnO}_3$ therefore depend on the fine interplay between the interactions that favor electron delocalization with ferromagnetism and those that favor electron localization with antiferromagnetism. The vast majority of theoretical models are focused on CMR, the FM metallic and the PM insulating state. They can be divided into models based on (i) double exchange, (ii) Anderson localization, and (iii) polarons (see Refs. [34,35]). To date, however, none of these have been successful to quantitatively capture the CMR and to fully explain the origin of the PM insulating state.

At present, it is believed that the key for understanding the manganites is phase separation on the nanoscale [35–38]—the coexistence of nanometer-size spatial regions, i.e., nanoclusters, with different electronic orders. In such a scenario, close to the boundary between the FM metallic and the PM or CO/AFM insulating phase, the system consists of FM nanoclusters embedded in a PM or CO/AFM matrix. Based on the double exchange, e_g electrons can move only within the FM nanoclusters with magnetization oriented parallel to the e_g spin. Easy alignment and/or growth of the FM nanoclusters in a magnetic field then leads to a large increase in conductivity and eventually to metallic conduction, i.e., to CMR. The CMR and metal–insulator transitions in manganites are therefore thought to rely on cluster-dynamics, rather than on the dynamics of atomic magnetic moments. Indeed, theories based on small FM clusters of randomly oriented magnetizations seem to provide a considerable improvement in our understanding of the CMR and the associated FM metallic state [39–44]. The origin of the insulating behavior in the PM and CO/AFM phases, however, still remains unresolved.

To gain insight into the origin of the insulating behavior in manganites, we recently focused on the poorly explored insulating CO/AFM part of the phase diagram $x > 0.5$ (Figure 1a). Our study on $\text{La}_{1-x}\text{Ca}_x\text{MnO}_3$ thin films indicated that dc resistivity follows the

Mott three-dimensional (3D) variable-range-hopping (VRH) mechanism, which implies the crucial role of structural disorder in driving the insulating behavior through the Anderson localization of conducting e_g electrons [45]. To further explore these ideas, here we conduct a dc transport and magnetization study on polycrystalline (ceramic) $\text{La}_{1-x}\text{Ca}_x\text{MnO}_3$ samples, where the level of structural disorder can be controlled by the grain size. We focus on the very boundary between the FM metallic and CO/AFM insulating phases $x = 0.5$, where the grain size is known to have a large impact on the stability of the CO/AFM phase [46–52]. Our results show the presence of the 3D VRH in accordance with the thin film study [45] and the coexistence of both FM and CO/AFM phases. Reducing the grain size leads to the suppression of the CO/AFM state and a growth of the FM contribution. The accompanying increase in structural disorder surprisingly induces a disappearance of the VRH and pushes the system towards the metallic state, which is opposite to the Anderson localization. Such counter-intuitive behavior is discussed here in light of the standard core-shell model and recent theories of electron localization in the presence of structural disorder and electron–electron or electron–lattice interactions [53–56] that have until now not been considered in manganites.

2. Materials and Methods

Ceramic samples of half-doped manganite $\text{La}_{0.5}\text{Ca}_{0.5}\text{MnO}_3$ were prepared by the sol–gel method which is based on the esterification and polymerization reaction of ethylene glycol (EG) and ethylenediaminetetraacetic acid (EDTA). The stoichiometric amounts of La_2O_3 , CaCO_3 and 50 % $\text{Mn}(\text{NO}_3)_2$ solution were used as starting materials. La_2O_3 and CaCO_3 were converted into metal nitrates by adding nitric acid. These metal nitrates and excessive EDTA were dissolved in distilled water to obtain a clear solution with an initial molar ratio of $\text{La}:\text{Ca}:\text{Mn} = 1:1:2$. The pH of the solution was adjusted to 6–7 by adding ethylenediamine, and then an appropriate amount of EG was added to the solution. Subsequently, the solution was heated with stirring to evaporate most of the solvent water. The resultant gel precursors were decomposed at about 300 °C to obtain black precursor powder which was then separated into several parts and annealed at temperatures of 600, 1100 and 1280 °C to gain samples with average grain size approximately 40, 400 and 4000 nm, respectively, labelled hereafter as S40, S400 and S4000 (see Table 1).

Table 1. Structural properties of the $\text{La}_{0.5}\text{Ca}_{0.5}\text{MnO}_3$ samples obtained from SEM imaging and Rietveld fits. In all samples, the crystallites are significantly smaller than the grains, indicating the presence of many crystallites within each grain.

Sample Label	Grain Size (nm)	Crystallite Size (nm)	a (Å)	b (Å)	c (Å)
S4000	4100 ± 1400	301 ± 10	5.4099(3)	7.6240(4)	5.4183(3)
S400	400 ± 120	28 ± 3	5.464(2)	7.787(3)	5.504(2)
S40	43 ± 13	14 ± 2	5.502(3)	7.786(4)	5.424(3)

The crystal structure and surface morphology of the samples were thoroughly investigated at room temperature by X-ray powder diffraction and scanning electron microscopy (SEM), respectively. The X-ray powder diffraction data were collected with a Bruker D8 Discover diffractometer (Bruker AXS GmbH, Karlsruhe, Germany) equipped with a LYNX-EYE XE-T detector configured in a Bragg–Brentano geometry. Data were collected in 2θ range 30–80° with a step of 0.02° and Cu source with a wavelength of 1.54060 Å with Ni filter, 2.5° Soller slit and fixed slit at 0.4 mm. The slit opening in front of the detector was 6.5 mm, and the detector opening was 1.3°, resulting in an integrating time per step of 25 s. The crystallite size was determined by the Rietveld method using X’Pert Highscore Plus software 3.0 (Malvern Panalytical, Almelo, The Netherlands). Its algorithm utilizes the following formula for crystallite size determination: $D_i = \frac{180}{\pi} \frac{\lambda}{W_i - W_{st}}$, where λ is the wavelength of the radiation used (Cu in our case), W_i is the Caglioti parameter of the investigated phase which is refined within the structure refinement, and W_{st} is the Caglioti

parameter of the standard used to determine the instrumental broadening. The pseudo Voigt function was used in both cases, and LaB_6 was used as the standard refined under the same conditions as the measured samples. The variance of the crystallite size is described by: $\sigma^2(D_i) = \frac{A_D^2}{4(W_i - W_{st})^3} [\sigma^2(W_i) + \sigma^2(W_{st})]$, with A_D representing the constant $180\lambda/\pi$. FWHM values as such were not directly used in this procedure, but as stated above, refined Caglioti parameter W was taken instead.

The surface morphology and grain size were examined in a Jeol JSM-7800F field emission SEM instrument by collecting the secondary electrons at a working distance of about 10 mm and with an electron beam acceleration voltage of 10 kV. The grain size for each sample was determined as an average diameter value of 100 grains on the corresponding SEM image (for details see Appendix B).

Resistivity (ρ) was measured by the standard four-contact dc technique in the temperature (T) range 4.2–300 K. The current between 1 nA and 100 μA was applied along the long axis of the samples. The electrical contacts were made by applying silver paste directly to the sample surface. The contact resistance turned out to be around 10 times smaller than the 4-point sample resistance in the whole T -range, indicating a high quality of the contacts. The resistances above 1 G Ω for the most insulating S4000 sample at $T < 34$ K were determined by two contact current measurements using the picoammeter Keithley 6487 with voltage excitation up to 10 V. A good overlap between the four-contact and the two-contact measurement implies that the quality of the contacts does not deteriorate even at the lowest T , and therefore, the two-contact measurement gives a reliable value of the sample resistivity.

Magnetization (M) measurements were conducted using commercial Quantum Design MPMS XL-5 and MPMS 3 magnetometers in magnetic fields H up to 70 kOe and in the T -range 2–300 K. Zero-field cooled (ZFC) and field cooled (FC) $M - T$ curves were measured at 0.5 K/min in the field 100 Oe. The FC curves were recorded both during cooling and warming and are standardly labeled as FCC and FCW, respectively. The magnetic hysteresis $M - H$ curves were measured at fixed temperatures always from 70 to -70 kOe and back to 70 kOe. The initial $M - H$ curve from 0 to 70 kOe was measured only at 300 K while between the two temperatures the sample was kept in the maximum field 70 kOe.

3. Results

3.1. Structural Properties

The granular structure of the ceramic $\text{La}_{0.5}\text{Ca}_{0.5}\text{MnO}_3$ samples determined by SEM is shown in Figure 2. The average grain size for the three samples S4000, S400 and S40 studied is 4100 ± 1400 nm (Figure 2a), 400 ± 120 nm (Figure 2b) and 43 ± 13 nm (Figure 2c), respectively.

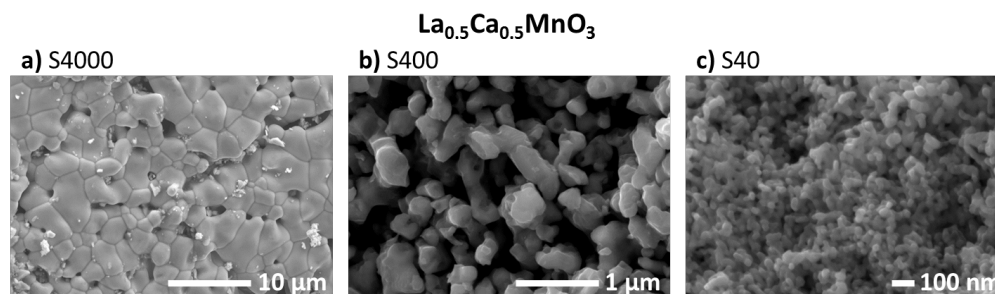


Figure 2. The surface morphology of the ceramic $\text{La}_{0.5}\text{Ca}_{0.5}\text{MnO}_3$ samples. SEM images obtained from: (a) S4000; (b) S400; and (c) S40 with the average grain size of 4100 ± 1400 , 400 ± 120 and 43 ± 13 nm, respectively. The scale bar is indicated in each image.

The dominant phase in all three samples determined by X-ray is $\text{La}_{0.5}\text{Ca}_{0.5}\text{MnO}_3$ with the space group P_{nma} . S4000 and S40 have a single phase, while S400 contains small amount of CaMnO_3 . The X-ray scans are shown in Figure 3, and unit cell parameters

as well as the crystallite sizes are listed in Table 1. Note that in all samples, each grain contains many crystallites and the smaller the grain size, the smaller the crystallite size. Therefore, going from S4000 to S40, the extrinsic structural disorder created by grain and crystallite boundaries drastically increases and is therefore expected to strongly influence the transport properties of our ceramic $\text{La}_{0.5}\text{Ca}_{0.5}\text{MnO}_3$ samples which is shown in the next section. In contrast to the extrinsic, the intrinsic structural disorder created by the La/Ca substitution is not expected to significantly change between the three samples. The same is true for any additional disorder coming from crystal defects and/or crystal impurities. For clarity from now on, we will mainly refer to the disorder created by grains but will keep in mind that crystallite boundaries, La/Ca substitution and crystal defects/impurities also contribute to the overall disorder.

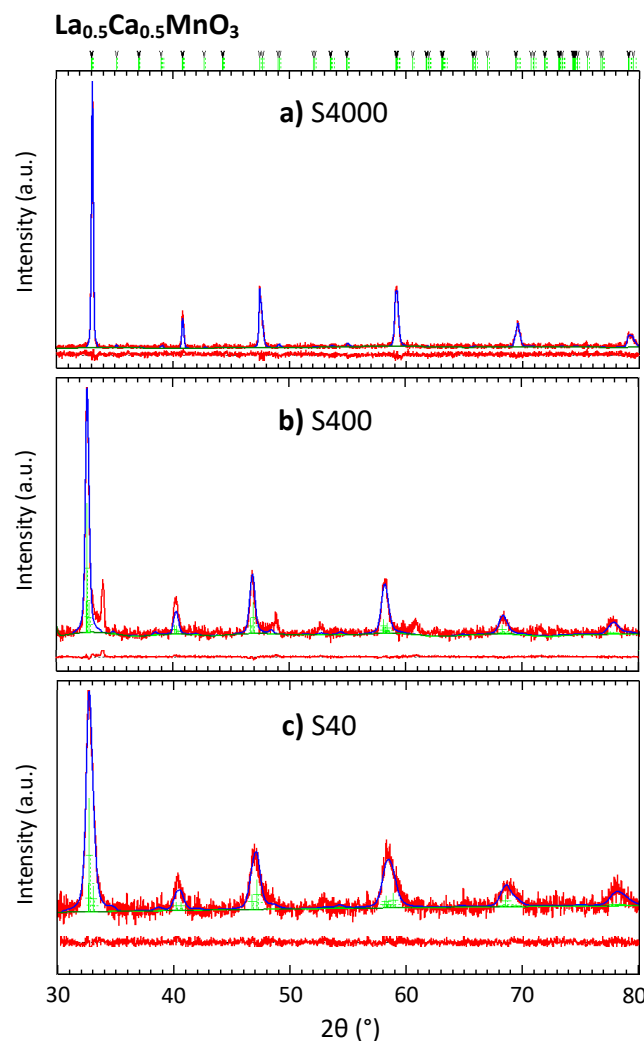


Figure 3. X-ray scans of the $\text{La}_{0.5}\text{Ca}_{0.5}\text{MnO}_3$ samples for: (a) S4000; (b) S400; and (c) S40. Red lines are the experimental data, blue lines are Rietveld fits, and green marks are the maximum positions. Corresponding residuals are shown below each X-ray spectrum. Several additional maximums for S400, approximately at 34° , 49° and 61° , not related to the P_{nma} structure of $\text{La}_{0.5}\text{Ca}_{0.5}\text{MnO}_3$ indicates the presence of small amounts of CaMnO_3 .

3.2. DC Resistivity

The values of the dc resistivity at room temperature $\rho_{300\text{K}}$ in the $\text{La}_{0.5}\text{Ca}_{0.5}\text{MnO}_3$ samples are approximately 6 m Ωcm , 1.5 Ωcm and 4.4 Ωcm for S4000, S400 and S40, respectively. This huge difference in $\rho_{300\text{K}}$ of three orders of magnitude between the samples illustrates the sensitivity of dc transport properties in $\text{La}_{0.5}\text{Ca}_{0.5}\text{MnO}_3$ to the microstructure. It seems

that there is a direct correlation between the ρ_{300K} value and the level of disorder related to the grain (and crystallite) boundaries. The most ordered S4000 sample has the smallest ρ_{300K} , while the most disordered S40 sample has the largest ρ_{300K} value. In a naïve picture, such behavior can be ascribed to additional electron scattering on grain (and crystallite) boundaries which are abundant in S40 and rare in S4000 (see Table 1). However, taking into account that charge transport in $\text{La}_{0.5}\text{Ca}_{0.5}\text{MnO}_3$ close to room temperature possibly takes place via polaron hopping [45,57,58], a more complex explanation would be more appropriate which is beyond the scope of the present study.

The difference between the $\text{La}_{0.5}\text{Ca}_{0.5}\text{MnO}_3$ samples is even more pronounced in the T -dependence of resistivity shown in Figure 4a. Here the resistivities are normalized to the values at 300 K to emphasize the difference in T -evolution. As we can see, all samples show insulator-like behavior (negative $d\rho/dT$) with the ρ/ρ_{300K} ratio spanning more than 10 orders of magnitude at the lowest T . Such a large difference, once again, illustrates the sensitivity of dc transport properties to the sample microstructure. Clear temperature hysteresis of resistivity is visible only for S4000 in the T -range 100–220 K, with the resistivity in cooling being lower than the one in warming. A matching temperature hysteresis is also found in magnetization (see the next section) with indications of a slow relaxation in time. This implies that during cooling the system stays trapped in a metastable state. As we can see, the sample S4000 with the largest grains has the steepest $d\rho/dT$, i.e., it shows the most pronounced insulating behavior. On the other hand, the sample S40 with the smallest grains shows the weakest insulating behavior. This implies that with reducing the grain size, i.e., with increasing structural disorder, the system is pushed towards a metallic state. Such a counter-intuitive behavior will be discussed in Section 4.

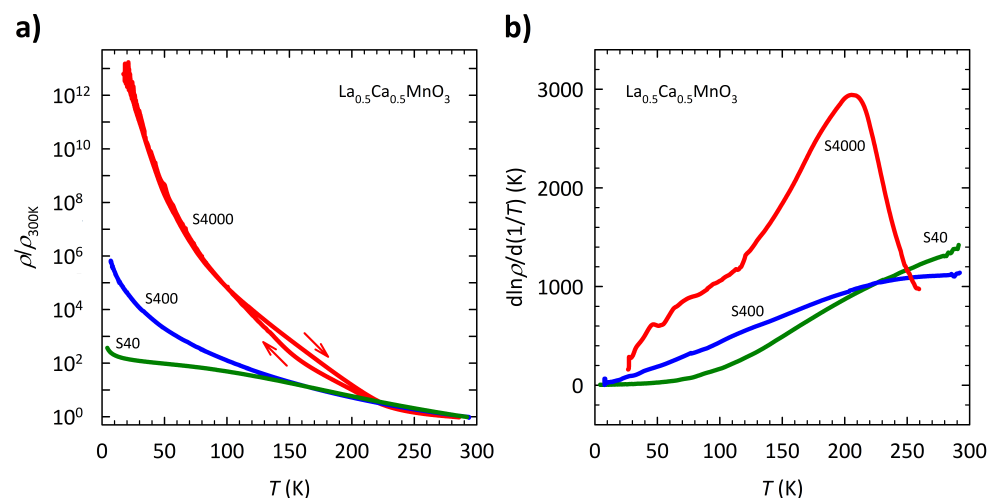


Figure 4. (a) DC resistivity and (b) its logarithmic derivative $d\ln\rho/d(1/T)$ as a function of temperature for the $\text{La}_{0.5}\text{Ca}_{0.5}\text{MnO}_3$ samples: S4000 (red line), S400 (blue line) and S40 (green line). The resistivities are normalized to the room temperature values to emphasize the difference in the T -evolution for different samples. The arrows indicate cooling and warming. The $d\ln\rho/d(1/T)$ curve for S4000 is shown only in warming for clarity.

Figure 4b shows the temperature dependence of the logarithmic resistivity derivative $d\ln\rho/d(1/T)$ for all three samples. The clear maximum in $d\ln\rho/d(1/T)$ at $T \approx 210$ K for S4000 is ascribed to the phase transition from the PM insulating to the CO insulating state (CO transition), expected from the conventional phase diagram shown in Figure 1a. Such a maximum in $d\ln\rho/d(1/T)$ is typical for $\text{La}_{1-x}\text{Ca}_x\text{MnO}_3$ compounds in the CO/AFM insulating part of the phase diagram $x > 0.5$, and as shown in Refs. [45,59], the position of the $d\ln\rho/d(1/T)$ maximum agrees well with the temperature at which the CO transition is expected according to the phase diagram. For clarity, in Figure 4b, $d\ln\rho/d(1/T)$ is shown only for warming. The cooling curve shows a similar maximum at the same T with an additional feature at a lower T which is related to the hysteretic behavior. The large width

of the maximum in $d\ln\rho/d(1/T)$ for S4000 indicates that there is no long-range CO, i.e., that CO occurs only at short range. As can be seen in Figure 4b, going from S4000 to S400 the maximum in $d\ln\rho/d(1/T)$ becomes significantly broader and flatter, while for S40 it becomes indiscernible. Together with the sharp drop in resistivity, this is a strong indication that reducing the grain size suppresses the CO/AFM phase.

The logarithmic resistivity derivative $d\ln\rho/d(1/T)$ shown in Figure 4b is not constant in temperature for any of the samples, indicating the absence of conventional activated behavior across an energy gap $\rho(T) \propto \exp(\Delta/T)$. A detailed analysis showed that the insulator-like behavior in S4000 at low- T can be best fitted to the standard Mott 3D VRH mechanism $\rho(T) \propto \exp(T_0/T)^{1/4}$, where T_0 is a characteristic Mott's activation energy [60]. In general, VRH is typical for disordered systems in which a strong scattering of electrons caused by disorder leads to the localization of electronic states at the Fermi level E_F . In these so called Anderson insulators, a charge transport takes place via hopping of electrons among the localized states at E_F not only between nearest neighbors but also of variable range. This mechanism of transport can lead to insulating behavior despite the absence of an energy gap at E_F . In strongly correlated systems such as manganites, however, the situation becomes more complicated since the disorder-induced localized states may coexist with the energy gap opened by strong electron–electron interactions [53–55] or with the mobility gap opened by strong electron/lattice coupling [56], which will be addressed in Section 4. In case of manganites, the presence of VRH implies that a conducting e_g electron hops between spatially distant Mn^{3+} and Mn^{4+} .

Figure 5a shows the temperature dependence of resistivity for all samples on a $\log\rho - T^{-1/4}$ plot, suitable for the 3D VRH mechanism which should then follow a straight line. Again, only the warming curve for S4000 is shown for clarity. As we can see, $\rho(T)$ in warming for S4000 follows the 3D VRH below the CO transition in a broad T -range from $T \approx 150$ K down to $T \approx 40$ K and increases almost eight orders of magnitude. The cooling curve follows the 3D VRH in a narrower T -range ≈ 120 –40 K, i.e., below the hysteretic region, where it overlaps with the warming curve. S400 and S40, though showing insulator-like behavior, do not fit well with the 3D VRH mechanism (see Appendix C).

Interestingly, the disappearance of the VRH with reducing the grain size is accompanied by the strong suppression of the CO/AFM phase (Figures 4b and 5a), implying a close relationship between them (see Section 4 for discussion). The suppression of the CO/AFM state with reducing the grain size has been well documented in the literature for the half-doped $La_{0.5}Ca_{0.5}MnO_3$ studied here [46–52], as well as for some other dopings such as $La_{0.4}Ca_{0.6}MnO_3$ [61,62] and $La_{0.25}Ca_{0.75}MnO_3$ [63] and other compositions such as $Pr_{0.5}Ca_{0.5}MnO_3$ [64,65] and $Nd_{0.5}Ca_{0.5}MnO_3$ [66]. Such behavior has been ascribed to surface effects at the grain boundaries, which destabilize the bulk long-range CO/AFM order and which become progressively more pronounced with the increase of the surface to volume ratio caused by the reduction in the grain size. As a consequence, the bulk CO/AFM state is confined only to the interior of the grains, while the grain boundaries are predominantly FM and consist of FM nanoclusters. This is the so-called core–shell model, where the core represents the CO/AFM interior of a grain, while the shell represents the FM grain boundary, schematically shown in Figure 5b. It is therefore expected that S40 with the smallest grains and a lot of grain boundaries has the largest fraction of the FM nanoclusters, while S4000 with the largest grains and few grain boundaries has the smallest fraction of the FM nanoclusters. To verify the validity of these conclusions, we performed a systematic magnetization study which is shown in the next subsection.

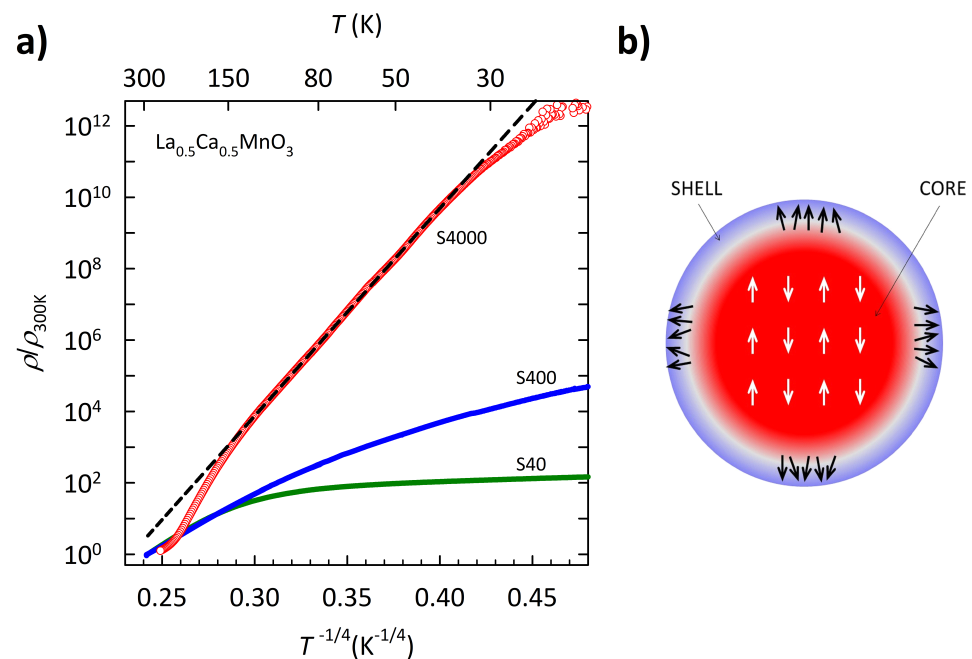


Figure 5. (a) $\log \rho - T^{-1/4}$ plot of the normalized resistivity, suitable for the Mott 3D VRH mechanism, for the $\text{La}_{0.5}\text{Ca}_{0.5}\text{MnO}_3$ samples: S4000 (red circles), S400 (blue line) and S40 (green line). Black dashed line is a fit to the 3D VRH $\rho(T) \propto \exp(T_0/T)^{1/4}$. Only the warming curve is shown for S4000 for clarity. (b) Schematic representation of the core–shell model in $\text{La}_{0.5}\text{Ca}_{0.5}\text{MnO}_3$, where the core of a grain is CO/AFM, and the shell is predominantly FM (see text).

3.3. Magnetization

Magnetization curves of the $\text{La}_{0.5}\text{Ca}_{0.5}\text{MnO}_3$ samples in the standard ZFC and FC protocols are shown in Figure 6. Sharp peak in the ZFC curve and a sudden jump in the FCC and FCW curves at $T \approx 40$ K for S4000 share a striking resemblance with the behavior of magnetization in Mn_3O_4 around its ferrimagnetic transition at $T \approx 43\text{--}48$ K [67,68]. It is known that during the sample synthesis, small amounts of Mn_3O_4 phase often appear within a manganite sample [69–71]. We therefore conclude that the behavior of magnetization for S4000 below ≈ 40 K is entirely extrinsic and related to small amounts of the Mn_3O_4 phase rather than to an intrinsic re-entrant spin glass transition, commonly reported in the literature [64,72–74]. (The absence of the re-entrant spin glass transition is additionally confirmed with the ac susceptibility measurements shown in Appendix A.) A rough estimate for the fraction of the Mn_3O_4 phase in S4000 can be obtained from the ratio of the magnetization measured in S4000 and the one measured in pure Mn_3O_4 . Taking the value $M = 0.3$ emu/g for S4000 from Figure 6a, and $M = 4.5$ emu/g for Mn_3O_4 from Ref. [68], both for the FC curves in $H = 100$ Oe at the lowest T , we obtain around 7% of Mn_3O_4 . Such a small fraction of Mn_3O_4 could not be detected by our X-ray measurements.

The absence of sharp features in the ZFC and FCC/FCW curves in all samples (except the extrinsic feature related to Mn_3O_4 in S4000) indicates that there are no ‘clean’ magnetic phase transitions which one would naïvely expect from the phase diagram in Figure 1. (The same conclusion can be drawn from the corresponding ac susceptibility, a technique which is even more sensitive for the detection of phase transitions, shown in Appendix A.) On the other hand, such behavior is consistent with the phase separation, i.e., the existence of FM and CO/AFM clusters that appear below some critical temperature [35–38]. In addition, there is a significant difference between the ZFC and FCC/FCW curves which we associate with the presence of FM nanoclusters. The FCC and FCW curves are not identical only in the case of S4000, which results in a pronounced thermal hysteresis in the same T -range 100–220 K where the hysteretic behavior of dc resistivity occurs (compare Figures 4a and 6a). The hysteretic behavior is probably related to the CO transition, visible only for S4000 as a

maximum in resistivity derivative that nicely coincides with the maximum in ZFC, FCC and FCW curves at $T \approx 220$ K (compare Figures 4b and 6a). Here it is important to recall that the magnetization and dc resistivity do not probe the same electrons in $\text{La}_{0.5}\text{Ca}_{0.5}\text{MnO}_3$, since the former is related to the core t_{2g} electrons, while the latter is related to the conducting e_g electrons. The coinciding features in magnetization and dc resistivity, therefore, confirm the expected strong coupling between the t_{2g} and e_g electrons.

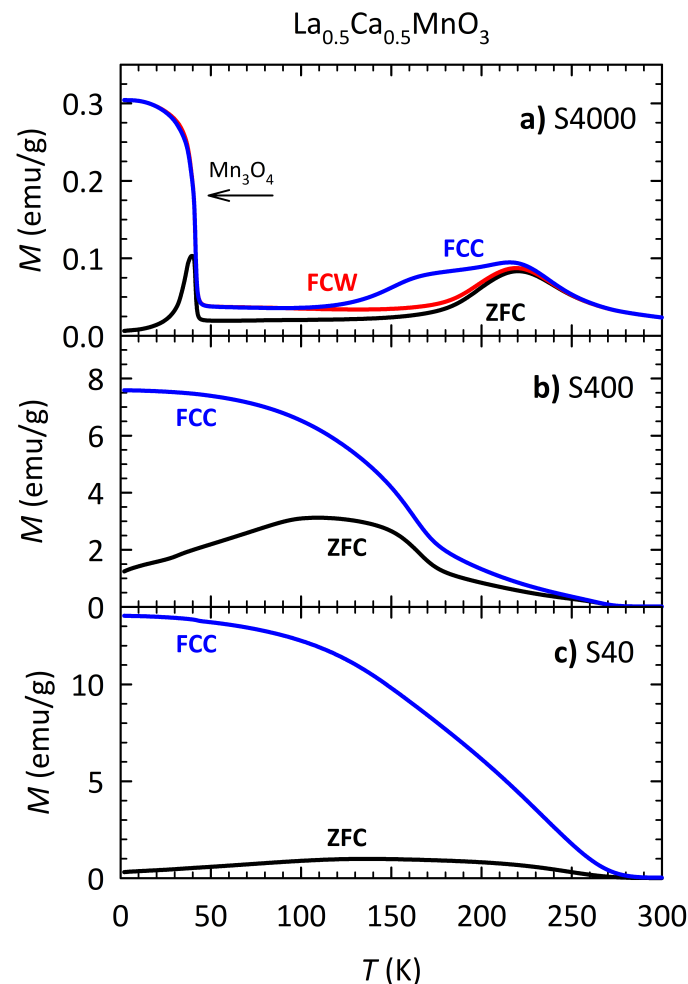


Figure 6. Standard ZFC and FC magnetization curves in $H = 100$ Oe for the $\text{La}_{0.5}\text{Ca}_{0.5}\text{MnO}_3$ samples: (a) S4000; (b) S400; and (c) S40. In the case of S4000, the FCC and FCW curves do not overlap and are indicated by the blue and red lines, respectively. In the case of S400 and S40 the FCC and FCW curves are identical (not shown) which was confirmed on other samples. The ZFC curves in all three panels are shown by the black lines. The sharp peak in ZFC and sudden jump in FCC and FCW curves at $T \approx 40$ K for S4000 are extrinsic and come from a tiny amount of Mn_3O_4 phase which often occurs during the sample synthesis [69–71].

As we can see in Figure 6, the FCC curve at low T has the highest value for S40 and the lowest for S4000, indicating that S40 has the largest and S4000 the smallest amount of FM nanoclusters in accordance with the expectation based on the core-shell model introduced in the previous section (see Figure 5). The same conclusion can be drawn from magnetic hysteresis loops shown in Figure 7. As can be seen in Figure 7a, the hysteresis loop at the lowest temperature $T = 2$ K for S40 closes at $H \approx 2$ kOe, reaching a value $M \approx 1.5 \mu_B/\text{Mn}$ where μ_B is the Bohr magneton. Beyond 2 kOe, the magnetization stays almost constant with a field as shown in the inset of Figure 7a. We ascribe such behavior to the FM part of the sample (the FM shells) which becomes fully saturated at 2 kOe. Taking into account that Mn^{3+} with four valence electrons contributes $4 \mu_B/\text{Mn}$, while Mn^{4+} with three valence

electrons contributes $3 \mu_B/\text{Mn}$, the theoretical saturation value for $\text{La}_{0.5}\text{Ca}_{0.5}\text{MnO}_3$ (which has equal number of Mn^{3+} and Mn^{4+}) would be $M = 3.5 \mu_B/\text{Mn}$ in the case of all Mn spins parallel to H . Here, only the contribution of valence electrons is considered since the orbital contribution of Mn^{3+} and Mn^{4+} is quenched [75]. The significantly lower measured saturation value therefore indicates that not all magnetic moments are aligned parallel to H which is in accordance with the proposed core-shell model. The measured value $M \approx 1.5 \mu_B/\text{Mn}$ then implies that only around 40% of the S40 sample is FM. The rest of the sample is CO/AFM and gives only a tiny contribution to the total magnetization as visible from the small but finite slope in the $M - H$ curve beyond the saturation (inset of Figure 7a).

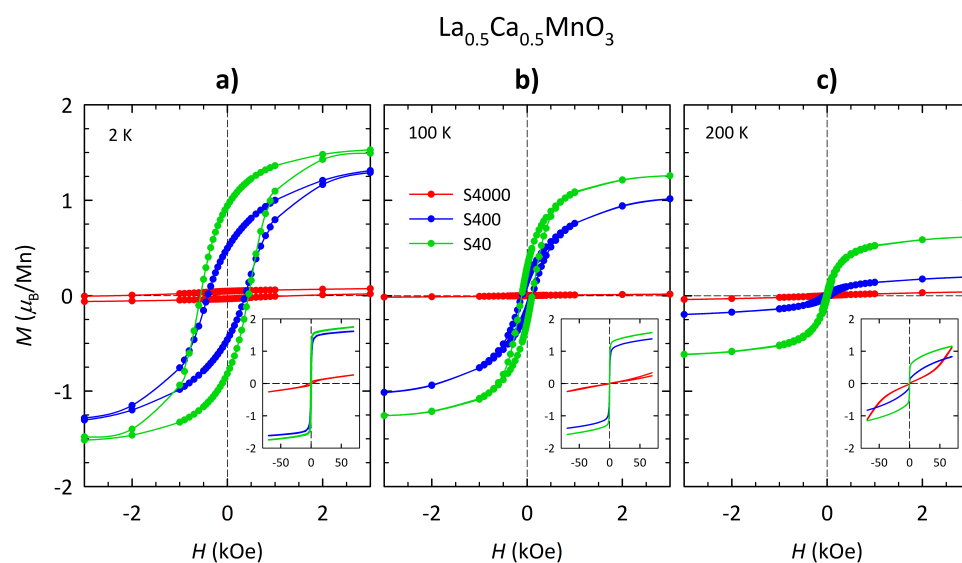


Figure 7. Magnetic hysteresis loops for the $\text{La}_{0.5}\text{Ca}_{0.5}\text{MnO}_3$ samples at: (a) 2 K; (b) 100 K; and (c) 200 K in the field range $-3 < H < 3$ kOe. All curves were measured in the FCC protocol. Magnetization is expressed in units of Bohr magneton μ_B per Mn atom. Red, blue and green symbols refer to the S4000, S400 and S40 sample, respectively. The full range of H is shown in insets. The low saturation values of M indicates that the FM fraction of $\text{La}_{0.5}\text{Ca}_{0.5}\text{MnO}_3$ is $< 5\%$, $\approx 35\%$ and $\approx 40\%$ for the S4000, S400 and S40 sample, respectively (see text).

Taking the measured values $M \approx 1.2 \mu_B/\text{Mn}$ and $M \approx 0.2 \mu_B/\text{Mn}$ from Figure 7a implies that around 35% of S400 and only about 5% of S4000 is FM at 2 K. The FM fraction of $\text{La}_{0.5}\text{Ca}_{0.5}\text{MnO}_3$ in S4000 is probably even lower since there is an additional contribution to the measured magnetization of the extrinsic ferrimagnetic Mn_3O_4 phase. Such a small FM fraction, together with the VRH and a clear signature of the CO transition (Figures 4b and 5a) in a sample with μm -sized grains (usually taken to represent the bulk behavior), implies that the insulating CO/AFM phase in $\text{La}_{1-x}\text{Ca}_x\text{MnO}_3$ is stable even at the very boundary with the FM metallic phase $x = 0.5$. This conclusion is in accordance with several previous reports [46,49,59].

The height and the width of hysteresis in S40 and S400 and consequently the FM fraction monotonously decrease with increasing T and become negligible on approaching room temperature (Figure 7) in accordance with the expectation based on the phase diagram. Here we recall that the hysteresis loops for all samples were measured during cooling from 300–4.2 K. Peculiar behavior is observed only in the case of S4000 within the thermal hysteretic region 220–100 K (Figure 6a) as indicated by the $M - H$ curve at 200 K that has an unexpected increase of slope at high fields (inset of Figure 7c), and the $M - H$ curve at 100 K that is not closed (inset of Figure 7b). The latter points towards slow time relaxations which imply that on cooling the system enters a metastable state with higher magnetization

(Figure 6a) and lower resistivity (Figure 4a), the origin of which is beyond the scope of the present study.

Finally, the coercive field at low T in all three samples is not completely symmetrical with respect to the origin, i.e., the hysteresis loops exhibit a small horizontal shift. Similar behavior was found also in $\text{Pr}_{0.5}\text{Ca}_{0.5}\text{MnO}_3$ ceramic samples [64] and was ascribed to the exchange bias effect related to a FM–AFM interface [64]. The presence of the exchange bias effect in our ceramic samples therefore provides additional indirect evidence for the coexistence of the AFM and FM regions, i.e., for the proposed core–shell formation depicted in Figure 5b. Direct imaging for the core–shell formation in manganites is still missing and would require studies based on local probes such as magnetic force microscopy at low temperatures.

4. Discussion

As mentioned in the introduction, the main goal of the present study is to shed more light on the origin of the insulating behavior in manganites $\text{La}_{1-x}\text{Ca}_x\text{MnO}_3$, specifically in the CO/AFM phase, which is still mostly not understood. Motivated by our previous study [45], which pointed towards the Anderson localization of conducting e_g electrons, here we explore the sensitivity of transport and magnetic properties in $\text{La}_{1-x}\text{Ca}_x\text{MnO}_3$ to the level of structural disorder controlled by the grain size. We focused on the very boundary between the FM metallic and CO/AFM insulating phases $x = 0.5$, where the grain size is known to strongly affect the stability of the CO/AFM phase [46–52]. Indeed, drastic changes in dc resistivity and magnetization were observed with varying the grain size, explained in detail in the previous sections. Here we will summarize these findings to build a picture of the insulating charge transport in the CO/AFM phase of $\text{La}_{1-x}\text{Ca}_x\text{MnO}_3$.

The absence of a clear transport gap, evident from the absence of a plateau in $\ln\rho/d(1/T)$ at low T (Figure 4b), immediately eliminates a simple explanation of the insulating behavior based only on the double exchange, the central interaction that governs the physics of manganites. Namely, according to the double exchange, one would expect that the insulating behavior in the CO/AFM state stems from the localization of e_g electrons caused by the prohibition of tunneling from Mn^{3+} to Mn^{4+} , the magnetic moments of which are aligned antiparallel. Such a scenario, however, would necessarily result in the opening of an energy gap at E_F since an e_g electron would need extra energy to hop to overcome the strong Hund interaction in contrast to the experiment. A very similar line of reasoning also excludes localization of e_g electrons by charge ordering as a key to insulating behavior, since here an e_g electron would need extra energy to overcome the strong electron–electron and/or Jahn–Teller interaction [25–27]. Therefore, the double exchange and/or charge ordering alone cannot explain the insulating behavior of the CO/AFM phase.

Indeed, the finite density of states at E_F is supported by the presence of the Mott 3D VRH transport mechanism in S4000 (Figure 5a) which implies the existence of localized energy states at E_F . Here the localization of conducting e_g electrons is caused by structural disorder which, in contrast to the localization caused by interactions, is not accompanied by the opening of an energy gap [54]. According to such an Anderson localization scenario, an increase in the level of structural disorder induced by the reduction in grain size from 4000 to 40 nm should result in a significant increase of resistivity. However, exactly the opposite behavior was observed in our ceramic samples (Figure 4a), indicating that the insulating behavior in the CO/AFM phase cannot stem from Anderson localization alone either. This conclusion should not be surprising, however, since the sudden delocalization of e_g electrons in the FM metallic phase obviously cannot be caused solely by the level of structural disorder which is not expected to change abruptly with small changes of x around $x = 0.5$ (Figure 1a). Moreover, the progressive delocalization of e_g electrons during the metal–insulator transition induced by a high magnetic field [45] cannot be related solely to the level of structural disorder which is not expected to change during the transition.

One solution to the above problem is to postulate that the localization of conducting e_g electrons in the CO/AFM phase stems from the combined effects of the structural disorder

and interactions. Indeed, by reducing the grain size not only does the VRH collapse, but also the fingerprint of the CO transition in dc resistivity disappears (see Figures 4b and 5a), suggesting that the electron–electron or electron–lattice interactions responsible for the long range CO/AFM order [25–27] also play a crucial role in the localization of conducting e_g electrons. The same conclusion can be drawn from the magnetization which shows that the disappearance of the VRH is accompanied by a significant increase of the FM contribution, i.e., a decrease of the AFM phase (Figure 6). Such behavior indicates that the grain size plays a delicate role in electron localization in $\text{La}_{0.5}\text{Ca}_{0.5}\text{MnO}_3$. On the one hand, it strengthens the localization by increasing the level of structural disorder, but on the other hand, it weakens the localization even more by destabilizing the CO/AFM phase.

There are several theoretical approaches to the problem of electron localization in the presence of both structural disorder and electron–electron interactions, the so called Mott–Anderson localization [53–55]. According to these models, the interplay between the electron–electron interactions and structural disorder is much more complex than one would expect, i.e., their effects do not necessarily reinforce each other in promoting insulating behavior. For example, for an intermediate disorder and a low interaction strength, the increase in electron–electron interactions can push the system towards the metallic state, rather than to the insulating state, by screening the disorder potential. For low disorder and intermediate interaction strength, the increase of structural disorder, instead of the insulating, can promote the metallic behavior by filling in the energy gap created by the strong electron–electron interactions. Nevertheless, for certain values of disorder and interaction strengths, the electron–electron interactions and structural disorder do reinforce each other, which would be in line with the experimental results presented here.

Even more appealing is a recent theory by Di Sante et al. [56] that focuses on the Anderson localization in the presence of electron–lattice coupling which always ‘antiscreens’ the disorder potential, i.e., strengthens the electron localization and therefore the insulating behavior. According to this theory, the electron–lattice coupling opens a mobility gap at E_F which separates the localized states around E_F from the delocalized states further away from E_F . (Note that there is no energy gap here since the density of states does not go to zero.) Here, the localization of conducting electrons is driven by a polaron formation, i.e., self-trapping by strong electron–lattice interactions and pinning by a disorder potential. Such a scenario could indeed be playing a role in manganites due to the strong Jahn–Teller effect believed to be responsible for polaronic conduction at high T [15–20] and for charge ordering at low T [25–27] as mentioned in the introduction. The observed VRH in S4000 would in this case be related to the states below the mobility gap which are localized by the combined effects of the structural disorder and strong electron–lattice coupling produced by the Jahn–Teller effect. The drastic decrease of resistivity with the reduction in grain size (Figure 4a), accompanied by the collapse of the VRH (Figure 5), could be ascribed to a weakening of the Jahn–Teller-induced polaron formation related to the suppression of the CO/AFM state (Figure 4b).

Interestingly, according to the same work by Di Sante et al. [56], close to the metallic state there is a regime with the so-called ‘bad insulator’ transport, which displays conductivity values below the Mott–Ioffe–Regel limit and an insulator-like temperature coefficient $d\rho/dT < 0$ with a finite intercept. Such peculiar behavior is often observed in strongly disordered metals [76] and here resembles the T -dependence found in the S400 and S40 ceramic samples (Figure 4a). It is reasonable to assume that with decreasing the grain size even further, $\text{La}_{0.5}\text{Ca}_{0.5}\text{MnO}_3$ would eventually end up in the metallic state. Indeed, Levy et al. [49] found the metallic behavior in $\text{La}_{0.5}\text{Ca}_{0.5}\text{MnO}_3$ ceramic samples after reducing the grain size down to 180 nm. The fact that the metallic behavior is absent in our sample S40 with significantly smaller grains illustrates the sensitivity of the transport properties of manganites to the sample preparation method that results in a significantly different level of disorder induced not only by the La/Ca substitution and grain boundaries, but also by, e.g., crystallite boundaries, which are usually ignored in the literature.

Finally, the fact that, besides the suppression of the CO/AFM phase, the collapse of the VRH is also accompanied by the growth of the FM fraction indicates the importance of the double exchange and the phase separation in manganites, which should be added to any theory of localization in manganites. The presence of the phase separation opens the possibility of a different explanation for the approach to the metallic state. If the growth of the FM fraction results in FM regions (clusters) big enough to host a Fermi surface, the metal–insulator transition becomes percolative in nature with spatially well-defined FM metallic and CO/AFM insulating regions. The drop of resistivity by more than 10 orders of magnitude between S4000 and S40 in Figure 4a without transition to the metallic state, i.e., without crossing the percolation threshold, however, cast some doubts on such a percolative nature. To resolve this issue, the studies based on local probes such as magnetic atomic force microscopy or scanning tunneling microscopy at low T are highly desirable.

5. Conclusions

In summary, our dc resistivity and magnetization study on $\text{La}_{0.5}\text{Ca}_{0.5}\text{MnO}_3$ ceramic samples clearly shows that the charge transport in the CO/AFM state at low temperatures is well described by the Mott 3D variable-range-hopping mechanism which strongly points towards the disorder-induced (Anderson) localization of conducting electrons. The drastic decrease of resistivity and collapse of the VRH with reducing the grain size, i.e., with increasing the disorder, however, drives the system in the opposite direction of the Anderson localization picture. The fact that the collapse of the VRH is accompanied by a strong suppression of the CO/AFM state implies a key role of interactions responsible for the long range order in localization of conducting electrons. In light of a recent theory of the Anderson localization in the presence of strong electron–lattice coupling, here we propose that the insulating behavior in the CO/AFM state of manganites possibly stems from polaron formation induced by the Jahn–Teller effect and enhanced by a disorder potential. The significant growth of the FM fraction with reducing the grain size, which originates from the surface effects on the grain boundaries, implies that the double exchange interaction and phase separation phenomena also play a role in the destruction of the VRH. More advanced theories of electron localization in the presence of multiple interactions would therefore be necessary to fully capture the origin of the insulating behavior in the CO/AFM state of manganites.

Author Contributions: Conceptualization, M.Č., T.I., S.T. and B.K.-H.; sample synthesis and characterization, T.Z., B.P.G.; X-ray measurements and analysis, T.K., Ž.S. and K.S.; SEM measurements and analysis, I.K.P. and M.P.; magnetization measurements and analysis, N.N. and Z.J.; dc resistivity measurements and analysis, D.R.G., T.I., M. Č., E.T., and M.B.; interpretation, M.Č., T.I., N.N., E.T., M.B., A.H., B.K.-H. and S.T.; writing—original draft preparation, M.Č.; writing—review and editing, M.Č., T.I. and N.N.; project administration, T.I. and S.T.; funding acquisition, T.I. and S.T. All authors have read and agreed to the published version of the manuscript.

Funding: This research was funded by the Croatian Science Foundation, Grants No. IP-2018-01-2730 and No. IP-2013-11-1011.

Institutional Review Board Statement: Not applicable.

Informed Consent Statement: Not applicable.

Data Availability Statement: Data is contained within the article.

Acknowledgments: We thank Ivan Balog, Mirta Herak, Goran Branković, and Jelena Vukašinić for elucidating discussions. We acknowledge support of project Cryogenic Centre at the Institute of Physics—KaCIF co-financed by the Croatian Government and the European Union through the European Regional Development Fund-Competitiveness and Cohesion Operational Programme (Grant No. KK.01.1.1.02.0012). We also acknowledge the support of project CeNIKS co-financed by the Croatian Government and the European Union through the European Regional Development Fund—Competitiveness and Cohesion Operational Programme (Grant No. KK.01.1.1.02.0013). I.K.P.

and M.P. acknowledge support from the University of Rijeka under the project number 18-144. Z.J. acknowledges also partial funding by Slovenian Research Agency (Grant No. P2-0348).

Conflicts of Interest: The authors declare no conflict of interest. The funders had no role in the design of the study; in the collection, analyses, or interpretation of data; in the writing of the manuscript, or in the decision to publish the results.

Appendix A. AC Susceptibility

Looking at the conventional phase diagram of $\text{La}_{1-x}\text{Ca}_x\text{MnO}_3$ shown in Figure 1a, we expect the phase boundary $x = 0.5$ to host both FM and CO/AFM phases in accordance with the widely accepted phase separation scenario [35–38]. Indeed, the magnetization measurements on $\text{La}_{0.5}\text{Ca}_{0.5}\text{MnO}_3$ ceramic samples shown in Figure 7 point towards the presence of two contributions, one related to the CO/AFM order placed in the interiors of grains and the other related to the FM nanoclusters placed at the grain boundaries as discussed in the main text. For completeness, here we present the corresponding magnetic ac susceptibility measurements.

Magnetic ac susceptibility is a very sensitive technique for studying magnetic properties, especially phase transitions and magnetic relaxation, and is complementary to the measurements in the static (dc) magnetic field. It measures the differential dM/dH response of the magnetization of a sample to an oscillating magnetic field $H(t) = h\cos(2\pi ft)$, where t is time, h is the field amplitude, and f is the field frequency. At low h , the magnetization oscillates with the same frequency as the field but generally with a phase shift θ , i.e., $M(t) = m\cos(2\pi ft - \theta)$. Magnetic ac susceptibility can therefore be expressed as a complex quantity $\chi' + i\chi''$, with the real component $\chi' = m\cos\theta/h$, which is in-phase with h and is related to the reversible magnetization processes, and the imaginary component $\chi'' = m\sin\theta/h$, which is out-of-phase with h and is related to the irreversible magnetization processes, i.e., the energy loss due to dissipation [77,78].

In the present study the magnetic ac susceptibility was measured using a high-resolution CryoBIND susceptometer with the driving ac field with f in the Hz–kHz range and $h = 0.9$ Oe. The measurements were performed in the T -range 4.2–320 K, during cooling and warming at the rate 1 K/min. No significant changes in χ' and χ'' were observed while changing the amplitude h of the ac field.

The measured χ' and χ'' as a function of T , normalized to the same arbitrary units by dividing with the mass of each sample, are shown in Figure A1. As we can see, χ' is significantly larger than χ'' for all three samples, indicating the expected dominance of reversible magnetization processes. Both components, χ' and χ'' , increase going from S4000 to S40 in accordance with the dc magnetization shown in Figure 6. Only in the case of S4000 do the cooling and the warming curves differ, resulting in a large thermal hysteresis in χ' and χ'' in approximately the same T -range where the hysteretic behavior of dc resistivity and dc magnetization occurs. No hysteretic behavior is observed in S400 and S40.

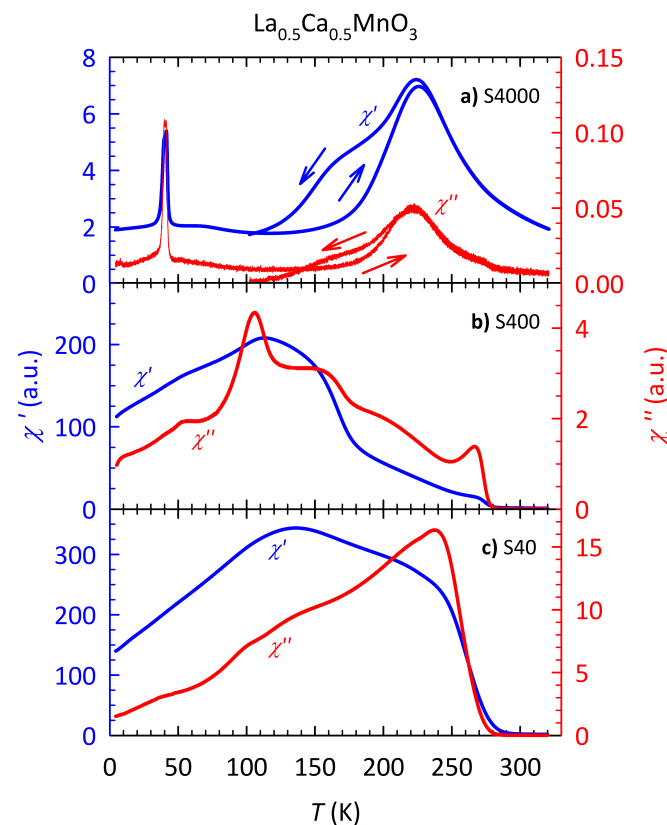


Figure A1. Magnetic ac susceptibility for the $\text{La}_{0.5}\text{Ca}_{0.5}\text{MnO}_3$ ceramic samples: (a) S4000; (b) S400; and (c) S40. Shown are the T -dependence of both the real χ' (blue lines, left axis), and imaginary χ'' (red lines, right axis) components, normalized to the mass of the sample. The cooling and warming curves differ only in the case of S4000.

The sharp peak in χ' and χ'' at $T \approx 40$ K for the bulk sample S4000 in Figure A1a is a clear signature of a phase transition, which is here attributed to the ferrimagnetic transition of the minority Mn_3O_4 phase, rather than to the intrinsic re-entrant spin glass transition commonly reported in the literature [64,72–74], as discussed in the main text. The absence of the spin glass transition is additionally confirmed by the frequency dependence of ac susceptibility on another $\text{La}_{0.5}\text{Ca}_{0.5}\text{MnO}_3$ sample from the same batch as S4000 shown in Figure A2. As we can see, the position of the sharp feature at $T \approx 40$ K does not change with f , which is in contrast to expectations for the spin glass transition [77–79]. The absence of additional sharp features in χ' and χ'' implies that there are no intrinsic ‘clean’ phase transitions, i.e., development of a ‘clean’ long-range order, in accordance with the phase separation into CO/AFM and FM regions.

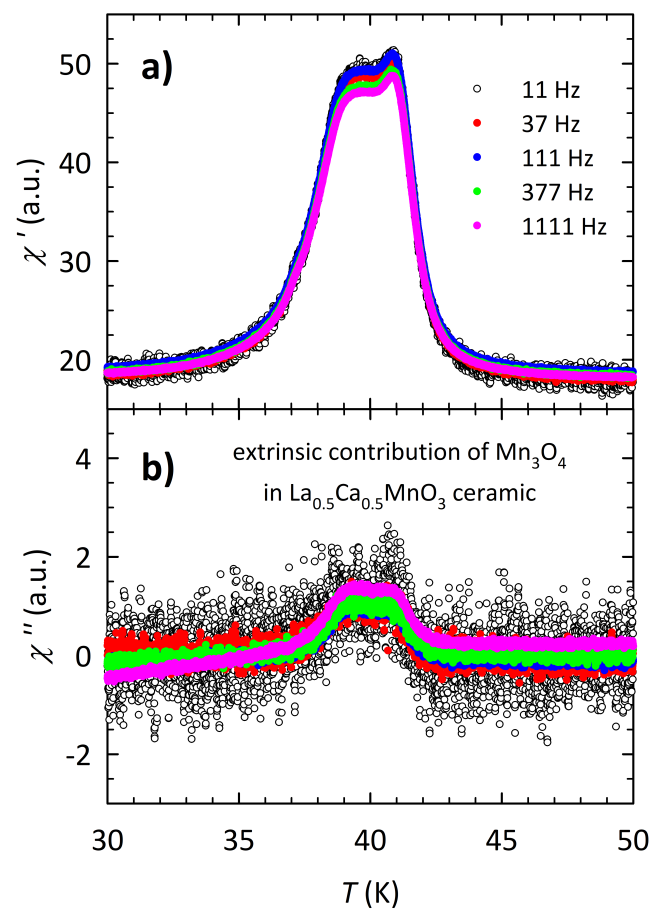


Figure A2. Temperature dependence of the (a) real χ' ; and (b) imaginary χ'' part of the ac susceptibility at low T for the $\text{La}_{0.5}\text{Ca}_{0.5}\text{MnO}_3$ ceramic sample (the same batch as S4000) at different frequencies. AC susceptibility depends only weakly on frequency.

Nevertheless, χ' and χ'' exhibit non-monotonous T -dependence with several broad maximums which point towards rich magnetic behavior in $\text{La}_{0.5}\text{Ca}_{0.5}\text{MnO}_3$. The maximum in χ' at $T \approx 220$ K for S4000 in Figure A1a coincides with the similar maximum in the ZFC and FCW curves in Figure 6a, as well as with the maximum in $\ln\rho/d(1/T)$ in Figure 4b related to the CO transition. One could therefore ascribe the maximum in χ' at $T \approx 220$ K to the development of the CO/AFM phase in the interior of grains in the S4000 sample. The finite value of χ'' with a very similar T -evolution to that of χ' , however, implies that the maximum at $T \approx 220$ K is related rather to the development of the FM nanoclusters at grain boundaries, since for the AFM phase, χ'' is expected to be zero [77,78].

The increase below $T \approx 280$ K and a smooth T -dependence of χ' in S400 and S40, accompanied by a significant change in χ'' with one or more broad maximums, is also attributed to the slow development of the FM nanoclusters at the grain boundaries. The rich structure in the T -dependence of χ'' for S400 indicates the presence of various irreversible magnetization processes probably related to the dynamics of the FM nanoclusters.

The negligible dependence of χ' and χ'' on the driving field amplitude h in all samples (not shown) indicates that all the features in the temperature plots of Figure A1 are still a part of linear response, which would not be expected if there was a conventional FM transition [77]. The dependence of χ' and χ'' on the driving field frequency is left for a future study. Especially interesting would be the frequency dependence for S4000 within the thermal hysteretic region 100–220 K, where we observed slow time evolution in the dc magnetization measurements, which points towards the presence of some form of a glassy (metastable) state.

Appendix B. Grain Size Distribution

As mentioned in the main text, the grain size of our ceramic samples was determined as an average diameter value of 100 grains on their corresponding SEM images. The grain size distributions for each sample are shown as histograms in Figure A3. The vertical black line represents the average grain size value for each sample.

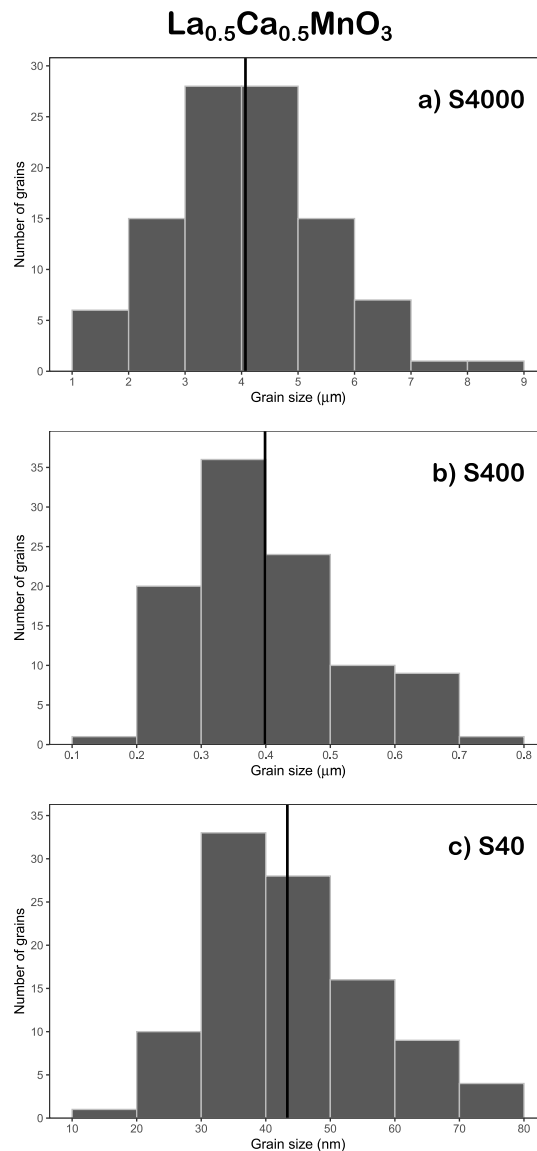


Figure A3. Grain size distribution in the $\text{La}_{0.5}\text{Ca}_{0.5}\text{MnO}_3$ ceramic samples: (a) S4000; (b) S400; and (c) S40. The average grain size values 4100 ± 1400 , 400 ± 120 and 43 ± 13 nm for S4000, S400 and S40, respectively, are indicated by the vertical black line.

Appendix C. Fitting of Variable-Range-Hopping Mechanism

As mentioned in the main text, the resistivity of the sample S4000 follows the 3D VRH in a large T -interval 40–150 K in which it increases almost eight orders of magnitude, evident from a linear dependence on a $\log \rho - T^{-1/4}$ scale (Figure 5a). Although at first sight it seems that there is a linear region on the $\log \rho - T^{-1/4}$ plot at high T (300–140 K), for the other two samples S400 and S40, as well as at low T (140–20 K) for S40, the resistivity in that case increases by only one order of magnitude, or even less, which indicates the absence of the strong exponential T -dependence expected for the 3D VRH. To illustrate this more explicitly, we follow the procedure outlined in several papers [80–84], where one starts from

the more general expression for resistivity $\rho \propto \exp(C/T)^p$, with C and p constant. Note that for $C = \Delta$ and $p = 1$ the previous equation reduces to the simple activated behavior, while for $C = T_0$ and $p = 1/4$ it recovers 3D VRH. To extract the exponent p , one defines a logarithmic resistivity derivative $W = -d(\ln\rho)/d(\ln T)$ which for the previous equation gives $p(C/T)^p$. The exponent p can then be obtained from the slope of $\ln W$ vs. $\ln T$.

The $\ln W$ – $\ln T$ plots for our ceramic samples S4000, S400 and S40 are shown in Figure A4. Although the data are somewhat noisy, we can clearly see that the slope p of $\ln W$ vs. $\ln T$ agrees with the expected value $1/4$ for 3D VRH only for S4000 in the T -range 150–40 K as stated in the main text. In the case of samples S400 and S40, not only is the value of the slope of $\ln W$ vs. $\ln T$ different from $1/4$, but also the sign of the slope is incorrect in almost the whole T -range of interest. We can therefore safely conclude that the resistivity of S400 and S40 does not follow the 3D VRH mechanism.

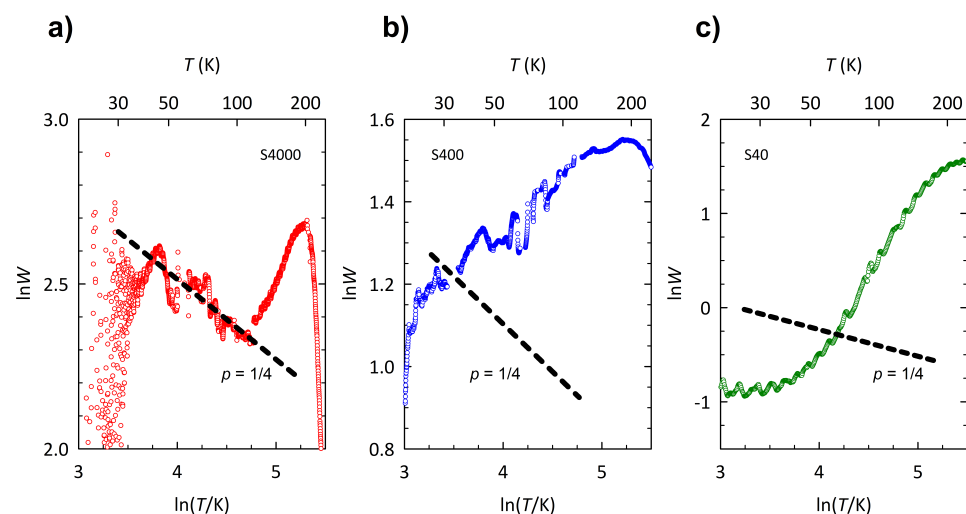


Figure A4. $\ln W$ vs. $\ln T$ for the $\text{La}_{0.5}\text{Ca}_{0.5}\text{MnO}_3$ ceramic samples: (a) S4000; (b) S400; and (c) S40, see text for details. Black dashed lines correspond to the slope expected for the 3D VRH ($p = 1/4$) and agree with the measured data only for S4000 in the T -range 150–40 K.

References

1. Rao, C.N.R. Transition Metal Oxides. *Annu. Rev. Phys. Chem.* **1989**, *40*, 291–326. [\[CrossRef\]](#)
2. Jonker, G.; Van Santen, J. Ferromagnetic compounds of manganese with perovskite structure. *Physica* **1950**, *16*, 337–349. [\[CrossRef\]](#)
3. Jin, S.; Tiefel, T.H.; McCormack, M.; Fastnacht, R.A.; Ramesh, R.; Chen, L.H. Thousandfold Change in Resistivity in Magnetoresistive La-Ca-Mn-O Films. *Science* **1994**, *264*, 413–415. [\[CrossRef\]](#) [\[PubMed\]](#)
4. Xiong, G.C.; Li, Q.; Ju, H.L.; Mao, S.N.; Senapati, L.; Xi, X.X.; Greene, R.L.; Venkatesan, T. Giant magnetoresistance in epitaxial $\text{Nd}_{0.7}\text{Sr}_{0.3}\text{MnO}_{3-\delta}$ thin films. *Appl. Phys. Lett.* **1995**, *66*, 1427–1429. [\[CrossRef\]](#)
5. Dagotto, E.; Hotta, T.; Moreo, A. Colossal magnetoresistant materials: The key role of phase separation. *Phys. Rep.* **2001**, *344*, 1–153. [\[CrossRef\]](#)
6. Nagaev, E. Colossal-magnetoresistance materials: Manganites and conventional ferromagnetic semiconductors. *Phys. Rep.* **2001**, *346*, 387–531. [\[CrossRef\]](#)
7. Salamon, M.B.; Jaime, M. The physics of manganites: Structure and transport. *Rev. Mod. Phys.* **2001**, *73*, 583–628. [\[CrossRef\]](#)
8. Imada, M.; Fujimori, A.; Tokura, Y. Metal–insulator transitions. *Rev. Mod. Phys.* **1998**, *70*, 1039–1263. [\[CrossRef\]](#)
9. Cheong, S.W.; Hwang, H.Y. Ferromagnetism vs. Charge/Orbital Ordering in Mixed-Valent Manganites. In *Colossal Magnetoresistive Oxides*; Tokura, Y., Ed.; Gordon and Breach: London, UK, 1999.
10. Kováčik, R.; Ederer, C. Effect of Hubbard U on the construction of low-energy Hamiltonians for LaMnO_3 via maximally localized Wannier functions. *Phys. Rev. B* **2011**, *84*, 075118. [\[CrossRef\]](#)
11. Nguyen, T.T.; Bach, T.C.; Pham, H.T.; Pham, T.T.; Nguyen, D.T.; Hoang, N.N. Magnetic state of the bulk, surface and nanoclusters of CaMnO_3 : A DFT study. *Phys. Condens. Matter* **2011**, *406*, 3613–3621. [\[CrossRef\]](#)
12. Zener, C. Interaction between the d -Shells in the Transition Metals. II. Ferromagnetic Compounds of Manganese with Perovskite Structure. *Phys. Rev.* **1951**, *82*, 403–405. [\[CrossRef\]](#)
13. Anderson, P.W.; Hasegawa, H. Considerations on Double Exchange. *Phys. Rev.* **1955**, *100*, 675–681. [\[CrossRef\]](#)
14. Kubo, K.; Ohata, N. A Quantum Theory of Double Exchange. I. *J. Phys. Soc. Jpn.* **1972**, *33*, 21–32. [\[CrossRef\]](#)

15. Ohtaki, M.; Koga, H.; Tokunaga, T.; Eguchi, K.; Arai, H. Electrical Transport Properties and High-Temperature Thermoelectric Performance of $(\text{Ca}_{0.9}\text{M}_{0.1})\text{MnO}_3$ ($M = \text{Y, La, Ce, Sm, In, Sn, Sb, Pb, Bi}$). *J. Solid State Chem.* **1995**, *120*, 105–111. [\[CrossRef\]](#)
16. Jaime, M.; Salamon, M.B.; Pettit, K.; Rubinstein, M.; Treece, R.E.; Horwitz, J.S.; Chrisey, D.B. Magnetothermopower in $\text{La}_{0.67}\text{Ca}_{0.33}\text{MnO}_3$ thin films. *Appl. Phys. Lett.* **1996**, *68*, 1576–1578. [\[CrossRef\]](#)
17. Jaime, M.; Hardner, H.T.; Salamon, M.B.; Rubinstein, M.; Dorsey, P.; Emin, D. Hall-Effect Sign Anomaly and Small-Polaron Conduction in $(\text{La}_{1-x}\text{Gd}_x)_{0.67}\text{Ca}_{0.33}\text{MnO}_3$. *Phys. Rev. Lett.* **1997**, *78*, 951–954. [\[CrossRef\]](#)
18. Palstra, T.T.M.; Ramirez, A.P.; Cheong, S.W.; Zegarski, B.R.; Schiffer, P.; Zaanen, J. Transport mechanisms in doped LaMnO_3 : Evidence for polaron formation. *Phys. Rev. B* **1997**, *56*, 5104–5107. [\[CrossRef\]](#)
19. Chun, S.H.; Salamon, M.B.; Han, P.D. Hall effect of $\text{La}_{2/3}(\text{Ca,Pb})_{1/3}\text{MnO}_3$ single crystals. *J. Appl. Phys.* **1999**, *85*, 5573–5575. [\[CrossRef\]](#)
20. Millis, A.J. Lattice effects in magnetoresistive manganese perovskites. *Nature* **1998**, *392*, 147–150. [\[CrossRef\]](#)
21. Wollan, E.O.; Koehler, W.C. Neutron Diffraction Study of the Magnetic Properties of the Series of Perovskite-Type Compounds $[(1-x)\text{La}, x\text{Ca}]\text{MnO}_3$. *Phys. Rev.* **1955**, *100*, 545–563. [\[CrossRef\]](#)
22. Ramirez, A.P.; Schiffer, P.; Cheong, S.W.; Chen, C.H.; Bao, W.; Palstra, T.T.M.; Gammel, P.L.; Bishop, D.J.; Zegarski, B. Thermodynamic and Electron Diffraction Signatures of Charge and Spin Ordering in $\text{La}_{1-x}\text{Ca}_x\text{MnO}_3$. *Phys. Rev. Lett.* **1996**, *76*, 3188–3191. [\[CrossRef\]](#) [\[PubMed\]](#)
23. Chen, C.H.; Cheong, S.W. Commensurate to Incommensurate Charge Ordering and Its Real-Space Images in $\text{La}_{0.5}\text{Ca}_{0.5}\text{MnO}_3$. *Phys. Rev. Lett.* **1996**, *76*, 4042–4045. [\[CrossRef\]](#) [\[PubMed\]](#)
24. Mori, S.; Chen, C.H.; Cheong, S.W. Pairing of charge-ordered stripes in $(\text{La,Ca})\text{MnO}_3$. *Nature* **1998**, *392*, 473–476. [\[CrossRef\]](#)
25. Zang, J.; Bishop, A.R.; Röder, H. Double degeneracy and Jahn-Teller effects in colossal-magnetoresistance perovskites. *Phys. Rev. B* **1996**, *53*, R8840–R8843. [\[CrossRef\]](#)
26. Mishra, S.K.; Pandit, R.; Satpathy, S. Mean-field theory of charge ordering and phase transitions in the colossal-magnetoresistive manganites. *J. Physics Condens. Matter* **1999**, *11*, 8561–8578. [\[CrossRef\]](#)
27. Hotta, T.; Malvezzi, A.L.; Dagotto, E. Charge-orbital ordering and phase separation in the two-orbital model for manganites: Roles of Jahn-Teller phononic and Coulombic interactions. *Phys. Rev. B* **2000**, *62*, 9432–9452. [\[CrossRef\]](#)
28. Zimmermann, M.v.; Hill, J.P.; Gibbs, D.; Blume, M.; Casa, D.; Keimer, B.; Murakami, Y.; Tomioka, Y.; Tokura, Y. Interplay between Charge, Orbital, and Magnetic Order in $\text{Pr}_{1-x}\text{Ca}_x\text{MnO}_3$. *Phys. Rev. Lett.* **1999**, *83*, 4872–4875. [\[CrossRef\]](#)
29. Hotta, T.; Takada, Y.; Koizumi, H.; Dagotto, E. Topological Scenario for Stripe Formation in Manganese Oxides. *Phys. Rev. Lett.* **2000**, *84*, 2477–2480. [\[CrossRef\]](#)
30. Goodenough, J.B. Theory of the Role of Covalence in the Perovskite-Type Manganites $[\text{La}, \text{M(II)}]\text{MnO}_3$. *Phys. Rev.* **1955**, *100*, 564–573. [\[CrossRef\]](#)
31. Birsan, E. The superexchange interaction influence on the magnetic ordering in manganites. *J. Magn. Magn. Mater.* **2008**, *320*, 646–650. [\[CrossRef\]](#)
32. Yi, H.; Yu, J.; Lee, S.I. Suppression of ferromagnetic ordering in doped manganites: Effects of the superexchange interaction. *Phys. Rev. B* **2000**, *61*, 428–431. [\[CrossRef\]](#)
33. Bao, W.; Axe, J.; Chen, C.; Cheong, S.W.; Schiffer, P.; Roy, M. From double exchange to superexchange in charge-ordering perovskite manganites. *Phys. B Condens. Matter* **1997**, *241–243*, 418–420. [\[CrossRef\]](#)
34. Dagotto, E. Open questions in CMR manganites, relevance of clustered states and analogies with other compounds including the cuprates. *New J. Phys.* **2005**, *7*, 67. [\[CrossRef\]](#)
35. Dagotto, E. *Nanoscale Phase Separation and Colossal Magnetoresistance*; Springer Series in Solid-State Sciences; Springer: Berlin/Heidelberg, Germany, 2003; Volume 136. [\[CrossRef\]](#)
36. Dagotto, E. Complexity in Strongly Correlated Electronic Systems. *Science* **2005**, *309*, 257–262. [\[CrossRef\]](#)
37. Nagaev, E.L. Lanthanum manganites and other giant-magnetoresistance magnetic conductors. *Physics-Uspokhi* **1996**, *39*, 781–805. [\[CrossRef\]](#)
38. Kagan, M.; Kugel, K.; Rakhmanov, A. Electronic phase separation: Recent progress in the old problem. *Phys. Rep.* **2021**, *916*, 1–105. [\[CrossRef\]](#)
39. Zhang, P.; Chern, G.W. Arrested Phase Separation in Double-Exchange Models: Large-Scale Simulation Enabled by Machine Learning. *Phys. Rev. Lett.* **2021**, *127*, 146401. [\[CrossRef\]](#)
40. Burgy, J.; Mayr, M.; Martin-Mayor, V.; Moreo, A.; Dagotto, E. Colossal Effects in Transition Metal Oxides Caused by Intrinsic Inhomogeneities. *Phys. Rev. Lett.* **2001**, *87*, 277202. [\[CrossRef\]](#)
41. Zhang, P.; Saha, P.; Chern, G.W. Machine Learning Dynamics of Phase Separation in Correlated Electron Magnets. *arXiv* **2020**, arxiv:2006.04205v1.
42. Luo, J.; Chern, G.W. Dynamics of electronically phase-separated states in the double exchange model. *Phys. Rev. B* **2021**, *103*, 115137. [\[CrossRef\]](#)
43. Pradhan, K.; Yunoki, S. Nanoclustering phase competition induces the resistivity hump in colossal magnetoresistive manganites. *Phys. Rev. B* **2017**, *96*, 214416. [\[CrossRef\]](#)
44. Burgy, J.; Moreo, A.; Dagotto, E. Relevance of Cooperative Lattice Effects and Stress Fields in Phase-Separation Theories for CMR Manganites. *Phys. Rev. Lett.* **2004**, *92*, 097202. [\[CrossRef\]](#) [\[PubMed\]](#)

45. Čulo, M.; Basletić, M.; Tafr, E.; Hamzić, A.; Tomić, S.; Fischgrabe, F.; Moshnyaga, V.; Korin-Hamzić, B. Magnetotransport properties of $\text{La}_{1-x}\text{Ca}_x\text{MnO}_3$ ($0.52 \leq x \leq 0.75$): Signature of phase coexistence. *Thin Solid Films* **2017**, *631*, 205–212. [\[CrossRef\]](#)
46. Freitas, R.; Ghivelder, L.; Levy, P.; Parisi, F. Magnetization studies of phase separation in $\text{La}_{0.5}\text{Ca}_{0.5}\text{MnO}_3$. *Phys. Rev. B* **2002**, *65*, 104403. [\[CrossRef\]](#)
47. Giri, S.K.; Nath, T.K. Suppression of Charge and Antiferromagnetic Ordering in $\text{La}_{0.5}\text{Ca}_{0.5}\text{MnO}_3$ Nanoparticles. *J. Nanosci. Nanotechnol.* **2011**, *11*, 4806–4814. [\[CrossRef\]](#)
48. Dhieb, S.; Krichene, A.; Boudjada, N.C.; Boujelben, W. Suppression of Metamagnetic Transitions of Martensitic Type by Particle Size Reduction in Charge-Ordered $\text{La}_{0.5}\text{Ca}_{0.5}\text{MnO}_3$. *J. Phys. Chem. C* **2020**, *124*, 17762–17771. [\[CrossRef\]](#)
49. Levy, P.; Parisi, F.; Polla, G.; Vega, D.; Leyva, G.; Lanza, H.; Freitas, R.; Ghivelder, L. Controlled phase separation in $\text{La}_{0.5}\text{Ca}_{0.5}\text{MnO}_3$. *Phys. Rev. B* **2000**, *62*, 6437–6441. [\[CrossRef\]](#)
50. Quintero, M.; Passanante, S.; Irurzun, I.; Goijman, D.; Polla, G. Grain size modification in the magnetocaloric and non-magnetocaloric transitions in $\text{La}_{0.5}\text{Ca}_{0.5}\text{MnO}_3$ probed by direct and indirect methods. *Appl. Phys. Lett.* **2014**, *105*, 152411. [\[CrossRef\]](#)
51. Gamzatov, A.G.; Batdalov, A.B.; Aliev, A.M.; Amirzadeh, P.; Kameli, P.; Ahmadvand, H.; Salamati, H. Influence of the granule size on the magnetocaloric properties of manganite $\text{La}_{0.5}\text{Ca}_{0.5}\text{MnO}_3$. *Phys. Solid State* **2013**, *55*, 502–507. [\[CrossRef\]](#)
52. Sarkar, T.; Ghosh, B.; Raychaudhuri, A.K.; Chatterji, T. Crystal structure and physical properties of half-doped manganite nanocrystals of less than 100-nm size. *Phys. Rev. B* **2008**, *77*, 235112. [\[CrossRef\]](#)
53. Byczuk, K.; Hofstetter, W.; Vollhardt, D. Mott-Hubbard Transition versus Anderson Localization in Correlated Electron Systems with Disorder. *Phys. Rev. Lett.* **2005**, *94*, 056404. [\[CrossRef\]](#) [\[PubMed\]](#)
54. Shinaoka, H.; Imada, M. Single-Particle Excitations under Coexisting Electron Correlation and Disorder: A Numerical Study of the Anderson–Hubbard Model. *J. Phys. Soc. Jpn.* **2009**, *78*, 094708. [\[CrossRef\]](#)
55. Aguiar, M.C.O.; Dobrosavljević, V.; Abrahams, E.; Kotliar, G. Critical Behavior at the Mott-Anderson Transition: A Typical-Medium Theory Perspective. *Phys. Rev. Lett.* **2009**, *102*, 156402. [\[CrossRef\]](#) [\[PubMed\]](#)
56. Di Sante, D.; Fratini, S.; Dobrosavljević, V.; Ciuchi, S. Disorder-Driven Metal-Insulator Transitions in Deformable Lattices. *Phys. Rev. Lett.* **2017**, *118*, 036602. [\[CrossRef\]](#) [\[PubMed\]](#)
57. Worledge, D.C.; Snyder, G.J.; Beasley, M.R.; Geballe, T.H.; Hiskes, R.; DiCarolis, S. Anneal-tunable Curie temperature and transport of $\text{La}_{0.67}\text{Ca}_{0.33}\text{MnO}_3$. *J. Appl. Phys.* **1996**, *80*, 5158–5161. [\[CrossRef\]](#)
58. Coey, J.M.D.; Viret, M.; von Molnár, S. Mixed-valence manganites. *Adv. Phys.* **1999**, *48*, 167–293. [\[CrossRef\]](#)
59. Zhou, H.D.; Zheng, R.K.; Li, G.; Feng, S.J.; Liu, F.; Fan, X.J.; Li, X.G. Transport properties of $\text{La}_{1-x}\text{Ca}_x\text{MnO}_3$ ($0.5 \leq x < 1$). *Eur. Phys. J. B* **2002**, *26*, 467–471. [\[CrossRef\]](#)
60. Mott, N.F.; Davis, E.A. *Electronic Processes in Non-Crystalline Materials*, 2nd ed.; International Series of Monographs on Physics, Clarendon Press: Oxford, UK, 2012.
61. Lu, C.L.; Dong, S.; Wang, K.F.; Gao, F.; Li, P.L.; Lv, L.Y.; Liu, J.M. Charge-order breaking and ferromagnetism in $\text{La}_{0.4}\text{Ca}_{0.6}\text{MnO}_3$ nanoparticles. *Appl. Phys. Lett.* **2007**, *91*, 032502. [\[CrossRef\]](#)
62. Rozenberg, E.; Auslender, M.; Shames, A.I.; Mogilyansky, D.; Felner, I.; Sominskii, E.; Gedanken, A.; Mukovskii, Y.M. Nanometer size effect on magnetic order in $\text{La}_{0.4}\text{Ca}_{0.6}\text{MnO}_3$: Predominant influence of doped electron localization. *Phys. Rev. B* **2008**, *78*, 052405. [\[CrossRef\]](#)
63. Zhang, T.; Zhou, T.F.; Qian, T.; Li, X.G. Particle size effects on interplay between charge ordering and magnetic properties in nanosized $\text{La}_{0.25}\text{Ca}_{0.75}\text{MnO}_3$. *Phys. Rev. B* **2007**, *76*, 174415. [\[CrossRef\]](#)
64. Zhang, T.; Dressel, M. Grain-size effects on the charge ordering and exchange bias in $\text{Pr}_{0.5}\text{Ca}_{0.5}\text{MnO}_3$: The role of spin configuration. *Phys. Rev. B* **2009**, *80*, 014435. [\[CrossRef\]](#)
65. Sarkar, T.; Mukhopadhyay, P.K.; Raychaudhuri, A.K.; Banerjee, S. Structural, magnetic, and transport properties of nanoparticles of the manganite $\text{Pr}_{0.5}\text{Ca}_{0.5}\text{MnO}_3$. *J. Appl. Phys.* **2007**, *101*, 124307. [\[CrossRef\]](#)
66. Rao, S.S.; Tripathi, S.; Pandey, D.; Bhat, S.V. Suppression of charge order, disappearance of antiferromagnetism, and emergence of ferromagnetism in $\text{Nd}_{0.5}\text{Ca}_{0.5}\text{MnO}_3$ nanoparticles. *Phys. Rev. B* **2006**, *74*, 144416. [\[CrossRef\]](#)
67. Boucher, B.; Buhl, R.; Perrin, M. Magnetic Structure of Mn_3O_4 by Neutron Diffraction. *J. Appl. Phys.* **1971**, *42*, 1615–1617. [\[CrossRef\]](#)
68. Narayani, L.; Jagadeesha Angadi, V.; Sukhdev, A.; Challa, M.; Matteppanavar, S.; Deepthi, P.; Mohan Kumar, P.; Pasha, M. Mechanism of high temperature induced phase transformation and magnetic properties of Mn_3O_4 crystallites. *J. Magn. Magn. Mater.* **2019**, *476*, 268–273. [\[CrossRef\]](#)
69. Filippetti, A.; Hill, N.A. First principles study of structural, electronic and magnetic interplay in ferroelectromagnetic yttrium manganite. *J. Magn. Magn. Mater.* **2001**, *236*, 176–189. [\[CrossRef\]](#)
70. Tomuta, D.G.; Ramakrishnan, S.; Nieuwenhuys, G.J.; Mydosh, J.A. The magnetic susceptibility, specific heat and dielectric constant of hexagonal YMnO_3 , LuMnO_3 and ScMnO_3 . *J. Physics Condens. Matter* **2001**, *13*, 4543–4552. [\[CrossRef\]](#)
71. Počuča-Nešić, M.; Marinković-Stanojević, Z.; Čotić-Smole, P.; Dapčević, A.; Tasić, N.; Branković, G.; Branković, Z. Processing and properties of pure antiferromagnetic h- YMnO_3 . *Process. Appl. Ceram.* **2019**, *13*, 427–434. [\[CrossRef\]](#)
72. Zhang, J.; Yu, L.; Cao, G.; Yu, Q.; Chen, M.; Cao, S. Cluster coexistence state in strongly correlation $\text{La}_{0.5}\text{Ca}_{0.5}\text{MnO}_3$ manganites. *Phys. B Condens. Matter* **2008**, *403*, 1650–1651. [\[CrossRef\]](#)

-
73. Cao, G.; Zhang, J.; Wang, S.; Yu, J.; Jing, C.; Cao, S.; Shen, X. Reentrant spin glass behavior in CE-type AFM $\text{Pr}_{0.5}\text{Ca}_{0.5}\text{MnO}_3$ manganite. *J. Magn. Magn. Mater.* **2006**, *301*, 147–154. [[CrossRef](#)]
 74. Lees, M.R.; Barratt, J.; Balakrishnan, G.; Paul, D.M.; Dewhurst, C.D. Low-temperature magnetoresistance and magnetic ordering in $\text{Pr}_{1-x}\text{Ca}_x\text{MnO}_3$. *J. Physics Condens. Matter* **1996**, *8*, 2967–2979. [[CrossRef](#)]
 75. Wang, K.F.; Wang, Y.; Wang, L.F.; Dong, S.; Li, D.; Zhang, Z.D.; Yu, H.; Li, Q.C.; Liu, J.M. Cluster-glass state in manganites induced by A-site cation-size disorder. *Phys. Rev. B* **2006**, *73*, 134411. [[CrossRef](#)]
 76. Lee, P.A.; Ramakrishnan, T.V. Disordered electronic systems. *Rev. Mod. Phys.* **1985**, *57*, 287–337. [[CrossRef](#)]
 77. Bałanda, M. AC Susceptibility Studies of Phase Transitions and Magnetic Relaxation: Conventional, Molecular and Low-Dimensional Magnets. *Acta Phys. Pol. A* **2013**, *124*, 964–976. [[CrossRef](#)]
 78. Topping, C.V.; Blundell, S.J. A.C. susceptibility as a probe of low-frequency magnetic dynamics. *J. Phys. Condens. Matter* **2019**, *31*, 013001. [[CrossRef](#)]
 79. Vincent, E.; Dupuis, V. Spin glasses: Experimental signatures and salient outcomes. In *Frustrated Materials and Ferroic Glasses*; Lookman, T., Ren, X., Eds.; Springer Series in Materials Science; Springer: Berlin/Heidelberg, Germany, 2017.
 80. Joung, D.; Khondaker, S.I. Efros-Shklovskii variable-range hopping in reduced graphene oxide sheets of varying carbon sp^2 fraction. *Phys. Rev. B* **2012**, *86*, 235423. [[CrossRef](#)]
 81. Khondaker, S.I.; Shlimak, I.S.; Nicholls, J.T.; Pepper, M.; Ritchie, D.A. Two-dimensional hopping conductivity in a δ -doped GaAs/ $\text{Al}_x\text{Ga}_{1-x}\text{As}$ heterostructure. *Phys. Rev. B* **1999**, *59*, 4580–4583. [[CrossRef](#)]
 82. Khondaker, S.; Shlimak, I.; Nicholls, J.; Pepper, M.; Ritchie, D. Crossover phenomenon for two-dimensional hopping conductivity and density-of-states near the Fermi level. *Solid State Commun.* **1999**, *109*, 751–756. [[CrossRef](#)]
 83. Chuang, C.; Puddy, R.; Lin, H.D.; Lo, S.T.; Chen, T.M.; Smith, C.; Liang, C.T. Experimental evidence for Efros–Shklovskii variable range hopping in hydrogenated graphene. *Solid State Commun.* **2012**, *152*, 905–908. [[CrossRef](#)]
 84. Zabrodskii, A.G. The Coulomb gap: The view of an experimenter. *Philos. Mag. B* **2001**, *81*, 1131–1151. [[CrossRef](#)]